Crystal nucleation mechanism in melts of short polymer chains under quiescent conditions and under shear flow

Muhammad Anwar, Joshua T. Berryman, and Tanja Schilling

Citation: The Journal of Chemical Physics **141**, 124910 (2014); doi: 10.1063/1.4896568
View online: http://dx.doi.org/10.1063/1.4896568
View Table of Contents: http://scitation.aip.org/content/aip/journal/jcp/141/12?ver=pdfcov
Published by the AIP Publishing

Crystal nucleation mechanism in melts of short polymer chains under quiescent conditions and under shear flow

Muhammad Anwar,[a] Joshua T. Berryman, and Tanja Schilling
Theory of Soft Condensed Matter Physics, Physics and Materials Research Unit, Université du Luxembourg, L-1511 Luxembourg, Luxembourg

(Received 18 July 2014; accepted 16 September 2014; published online 30 September 2014)

We present a molecular dynamics simulation study of crystal nucleation from undercooled melts of n-alkanes, and we identify the molecular mechanism of homogeneous crystal nucleation under quiescent conditions and under shear flow. We compare results for *n*-eicosane (C20) and *n*-pentacontahectane (C150), i.e., one system below the entanglement length and one above, at 20%–30% undercooling. Under quiescent conditions, we observe that entanglement does not have an effect on the nucleation mechanism. For both chain lengths, the chains first align and then straighten locally, then the local density increases and finally positional ordering sets in. At low shear rates the nucleation mechanism is the same as under quiescent conditions, while at high shear rates the chains align and straighten at the same time. We report on the effects of shear rate and temperature on the nucleation rates and estimate the critical shear rates, beyond which the nucleation rates increase with the shear rate. In agreement with previous experimental observation and theoretical work, we find that the critical shear rate corresponds to a Weissenberg number of order 1. Finally, we show that the viscosity of the system is not affected by the crystalline nuclei. © *2014 AIP Publishing LLC*. [http://dx.doi.org/10.1063/1.4896568]

I. INTRODUCTION

When a liquid is cooled below its crystal-liquid coexistence temperature, crystallites are formed. The shapes, sizes, and structures of these crystallites strongly influence the properties of the final, solidified material. This is particularly relevant for polymers, which generally do not reach a perfect single crystalline state but remain poly- or semicrystalline after cooling.

Polymer melts often flow during processing. Flow can change crystal nucleation and growth processes and hence affect the material properties of crystalline and semicrystalline plastics. Understanding crystallization in flowing polymer melts is thus a topic of technological relevance. But it is also a challenging topic from the point of view of basic theoretical physics, because relaxation in polymer melts occurs on a hierarchy of time-scales that spans several orders of magnitude. When discussing phase transitions in polymers, one inevitably deals with non-equilibrium processes, which can only to a very limited extent be described by quasi-equilibrium approaches. This fact poses a serious challenge to any attempt to theoretically model polymer crystallization.

In spite of intensive research efforts since the early 1940s, the molecular mechanism of polymer crystallization is still not completely understood.[1] Experimental research has been carried out using a wide range of techniques both, on polymers under quiescent conditions[2–11] and in external fields.[12–19] Crystallization rates and critical shear rates have been measured for different polymeric materials, the morphological features of the final crystal structure and the effect of molecular weight on the crystallization kinetics have been studied. But the primary nucleation mechanism has not been identified, because the short length- and time-scales on which it takes place are difficult to access experimentally.

Most theoretical approaches to flow induced crystallization are based on coarse-graining. Generally, sets of coupled differential equations for the time evolution of macroscopic quantities (e.g., the volume occupied by crystallites or the thickness of lamellae) are derived partly from the underlying microscopic theories, partly from balance conditions, and from considerations regarding the structure of effective free energy landscapes (see, e.g., Refs. 16 and 20–27). While undoubtedly useful, these models are inevitably semi-empirical. Coarse-graining requires approximations already in the equilibrium case. For the non-equilibrium case, in which one usually does not know the probability distributions of microstates according to which state-space averages would need to be taken, no systematic approach exists.

As the molecular length- and time-scales involved in nucleation and growth processes are below experimental resolution, and a theoretical approach is challenging because of the full non-equilibrium nature of the problem, computer simulations are a promising alternative method to solve the problem. McLeish and co-workers have over the past 15 years developed a comprehensive set of theoretical and computer simulation techniques and experimental model systems to study polymers under flow. To address crystallization they derived a kinetic Monte Carlo algorithm on the basis of kinetics extracted from the GLaMM model,[28] embedded it in a Brownian dynamics simulation[29,30] and extended this approach by a fast nucleation algorithm to compute nucleation rates.[31] This model captures many features of flow induced crystallization,

[a]muhammad.anwar@uni.lu

however, parts of it are based on an effective free energy picture, i.e., on the assumption of separating relaxation timescales and thus quasi-equilibrium.

Atomistic computer simulations have been used to study polymer crystallization under quiescent conditions[32–54,64] and under flow or large deformation.[55–63] Most of these studies focus on the growth process rather than the nucleation process, because nucleation is by definition a rare event (an event that occurs on a time-scale much larger than the time-scale of the local dynamics) and therefore difficult to tackle by atomistic simulation. Nucleation in short chain alkanes under quiescent conditions has nevertheless been simulated[32–37,39,40] and a scenario for the nucleation mechanism has been identified. (We will refer to this mechanism in detail in Secs. III, IV, and V.) The first direct computation of homogeneous nucleation rates in long chain alkanes by means of computer simulation has recently been presented by Rutledge and co-workers.[38] Their work was focussed on the nucleation and growth rates and the free energy landscape associated with the crystallization process rather than the microscopic mechanisms.

To our knowledge, there is no simulation study yet that resolves the molecular nucleation mechanism in polymers under shear. In this article, we present a detailed analysis of the formation of crystal nuclei from the melt in short chain alkanes under shear and in long chain alkanes under quiescent and shear conditions.

II. MODEL AND ORDER PARAMETERS

We have used a united atom model for polyethylene that has been proposed by Paul *et al.*[65] and later modified by Waheed *et al.*[51,66] We set the system parameters as in Ref. 66, with the exception of the Lennard-Jones cutoff radius which we set to $r_c^{LJ} = 2.5\sigma$. In order to carry out the simulations by means of the ESPResSo package[67] we implemented (and have made available) the dihedral-cosine potential and Lees Edwards periodic boundary conditions, which were not previously supported by ESPResSo.

We used several order parameters to identify the crystallites in the melt: for the analysis we split the long chains (C150) into segments of 15 monomers, while we regarded the short chains (C20) as single segments. Then we computed the radius of gyration R_g of each segment and the nematic order parameter S_2 of those segments that were involved in the formation of the critical nucleus. (A definition and detailed description of these parameters can be found in our previous work on C20.[40]) Further we measured the local alignment of bonds: Monomers within a radius $r_c = 1.4\sigma$ were considered as neighbours, where σ is the length scale set by the Lennard Jones interaction in the polymer model. Two neighbours i and j were considered as "aligned" if the chains they belonged to locally were almost parallel ($\theta_{ij} \leq 10^\circ$) . For a particle to be considered "crystalline," it had to have at least 13 aligned neighbours in case of C20 and 12 aligned neighbours in case of C150. These numbers were obtained by sampling the probability distributions of the number of aligned neighbours in the bulk crystal and the bulk liquid.

III. C150 UNDER QUIESCENT CONDITIONS

A. Simulation details

First we discuss the nucleation mechanism in a quiescent system of n-pentacontahectane(C150). We chose C150, because it has the minimum length for which we can capture the effects of entanglement on crystallization and observe a folded chain crystal structure (the entanglement length has been reported to be between 60 and 90 monomers[68–71]). We simulated 100 chains at 280 K, which corresponds to 30% supercooling. (For the model that we use, the equilibrium melting temperature of C150 is 396.4 K.[38]) We equilibrated the system at 500 K, i.e., well above the melting temperature. After equilibration we quenched the configurations from 500 K to 280 K and observed the nucleation event. We performed these simulations under constant pressure and constant temperature conditions. The pressure was fixed at 1 atm pressure.

The polymer model contains a Lennard-Jones-type interaction term. We therefore use Lennard Jones units to present our data (i.e., the particle mass m, the interaction energy k_BT, and resulting timescale $\tau = \sqrt{m\sigma^2/k_BT}$). Quantities which can be compared directly with the experimental results are presented in SI units. We used a Langevin dynamics based thermostat and barostat.[72] The friction coefficient γ used for the thermostat was $1.0\tau^{-1}$ and the piston mass for the barostat was $0.00001m$.

B. Nucleus formation

To determine the induction time and the size of the critical nucleus we performed a mean first passage time analysis[73] on 20 independent trajectories. (This method has been successfully applied to simulation data of nucleation in n-alkanes before.[36–38]) The values for the induction time t^* and the number of particles in the critical nucleus n^* are given in Table I. We find the nucleation rates to be in rough agreement with the results of Yi *et al.*[38] As we were using slightly different system sizes, different barostats and thermostats, small differences in the results were expected.

To analyze the nucleation mechanism, we identify in each trajectory those particles that are part of the critical nucleus at the nucleation time t_0. We then trace them backwards in time and compute their structural and orientational properties. We proceed backwards until the particles are indistinguishable from the melt particles. For 20 independent trajectories we compute the average radius of gyration R_g of all chain segments that are part of the nucleus at t_0, the nematic order S_2 of these chain segments, the average volume V of the Voronoi[74] cell associated to each particle that is part of the nucleus and its crystallinity order parameter. In Fig. 1, we show the relative variations of these quantities with respect to the values

TABLE I. Results of the mean first passage time analysis for C150 at 280 K.

Study	n^*	t^* (ns)	$I(10^{25}\,\mathrm{cm}^{-3}\,\mathrm{s}^{-1})$
Yi *et al.*[38]	143 ± 14	293 ± 19	1.47 ± 0.10
This work	87 ± 9	354 ± 41	0.72 ± 0.08

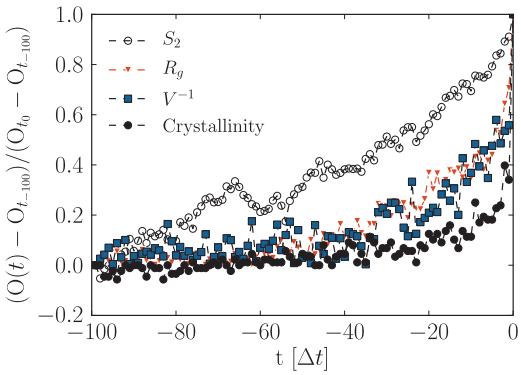

FIG. 1. Relative variation of several observables (O) from the melt to the formation of a critical nucleus, computed for those particles that are part of the nucleus at the nucleation time $t = t_0$: orientational order S_2 (black, open circles), radius of gyration R_g (red, triangles), the inverse of the Voronoi cell volume V (blue, squares), and the crystallinity order parameter (black, closed circles). The curves are averaged over 20 independent trajectories progressing backward in time from the nucleation time $t = t_0$ in steps $\Delta t = 100\,000\tau$ to $t = -100\Delta t$.

they had at $-100\Delta t$, where $\Delta t = 100\,000\tau$. (For comparison, changes in the absolute magnitude of these order parameters are shown in Appendix A.) When we advance from the supercooled melt towards the formation of the critical nucleus at t_0, we observe first an increase in the global orientational order S_2, then an increase in the radius of gyration of the segments and in the local density, and finally the crystal structure is formed.

We conclude that the nucleation mechanism in long, entangled chains is the same as in short, non-entangled chains: orientational ordering precedes straightening.[40]

Note that the Voronoi volume per particle in the nucleus does not deviate from its melt value until the very late stages of the nucleation process. We are thus not dealing with the spinodal decomposition assisted crystallization process that has been proposed by Olmsted *et al.*[25] Our results also stand in contrast to the scenario suggested by Doi *et al.* in which crystallization is initiated by an increase in the persistence length, followed by the alignment of the chains.[23,24]

In Fig. 2, we present snapshots of the formation of the critical nucleus at different times from $t = t_{-100}$ to $t = t_0$. The monomers that form the critical nucleus at t_0 are highlighted as large gray beads. The red color shows the segments of chains that participate with a single stem in the formation of the critical nucleus while blue, green, and orange indicate those chains which fold back and participate in the formation of the critical nucleus with more than one stem. For the case of folded chains we show complete chains instead of segments so that folds and tails can be identified. The images of the formation of the nucleus are consistent with the mechanism we proposed based on the values of S_2, R_g, V and the crystallinity order parameter (Fig. 1).

The critical nuclei consist of some chain segments (stems) from different chains and some from the same chain, which is folded. The primary nucleation mechanism is thus a combination of intramolecular and intermolecular mechanisms. Figure 3 shows the ratio of the number of stems to the number of chains. It is always larger than unity, i.e., there

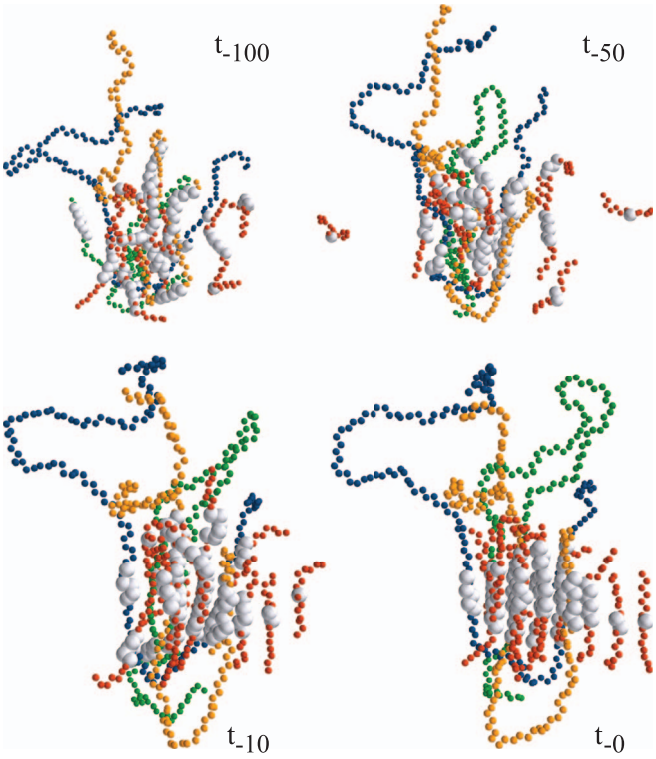

FIG. 2. Snapshots illustrating the nucleation mechanism. Large gray beads: monomers that form the critical nucleus at t_0. Red: segments of chains that participate with a single stem in the formation of the critical nucleus. Blue, green, and orange: chains which fold back and participate in the formation of the critical nucleus with more than one stem. For the case of folded chains we show complete chains instead of segments so that folds and tails can be identified.

are folded and non-folded chains in the clusters. This result agrees with the observations made by Yi *et al.*[38]

IV. C20 UNDER SHEAR

A. Simulation details

We studied the effect of shear on the nucleation rate and mechanism in *n*-eicosane (C20) by means of MD simulations at controlled temperature and constant volume, particle number and shear rate in a box with Lees-Edwards boundary

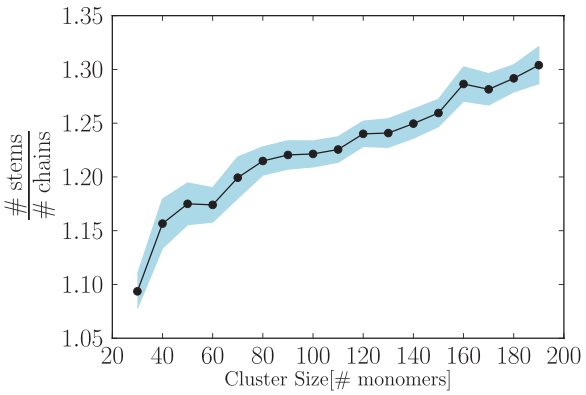

FIG. 3. Ratio of the number of stems to the number of chains against cluster size. The black curve (circles) shows the mean value and the light blue envelope shows the standard deviation.

TABLE II. Density of the metastable melt of *n*-eicosane at 1 atm pressure as a function of temperature.

Temperature (K)	Density (g/cm)^3	Reference
250	0.836	37[a]
255	0.833	37[b]
260	0.830	37[b]
265	0.828	37[a]
270	0.825	37[b]
275	0.822	37[b]
280	0.819	37[a]

[a] Densities taken from Yi *et al.*[37]
[b] Densities calculated by linear interpolation using data from Ref. 37.

conditions. The system consisted of 500 chains. We equilibrated it at 450 K, which is well above the melting temperature. (The equilibrium melting temperature of C20 in the simulation model we use is 310 ± 2 K,[37] which is in agreement with the experimentally observed value.) To set the density of the metastable melt at 1 atm pressure we used Table II.

We quenched the system from 450 K to 250 K, applied shear and observed the nucleation event. We ran simulations at seven different shear rates ranging from $\dot{\gamma} = 0.000001\tau^{-1}$ to $\dot{\gamma} = 0.01\tau^{-1}$ ($0.95 \times 10^{10}\,\mathrm{s}^{-1}$ to $0.95 \times 10^{6}\,\mathrm{s}^{-1}$). We also performed simulations at zero shear rate for comparison and we did not find any difference between the nucleation rate at the lowest non-zero shear rate and at zero shear rate. We used the dissipative particle dynamics (DPD) thermostat[75] with the friction coefficient $\gamma_{\mathrm{DPD}} = 1.0\tau^{-1}$. To ensure that steady state conditions were established sufficiently long before the onset of nucleation, we observed the velocity profile. In all simulations, the induction time was at least five times as long as the time needed to establish the steady state velocity profile.

In order to avoid the artefactual decoupling of the system from its periodic images remarked upon by Chatterjee[76] when using the DPD thermostat to treat a dissipative shear-flow, a modification to the pairwise dissipative DPD force $\vec{F}_{ij}^{D}$ was made:

$$\vec{v}_{ij}^{*\alpha} = \vec{v}_{ij}^{\alpha} - \frac{\dot{\gamma}}{L}\vec{r}_{ij}^{\beta}, \tag{1}$$

$$\vec{F}_{ij}^{D}(\vec{v}_{ij}^{\alpha}) := \vec{F}_{ij}^{D}(\vec{v}_{ij}^{*\alpha}), \tag{2}$$

where $\vec{v}_{ij}^{*\alpha}$ is laminar flow velocity, $\vec{v}_{ij}^{\alpha}$ is the pairwise velocity parallel to the laminar flow field, $\vec{r}_{ij}^{\beta}$ is the component of pairwise separation perpendicular to the flow field in the shear plane, and L is the length of simulation box. The effect of this modification is to exempt the laminar flow profile from dissipative forces, while allowing dissipation to operate as normal on the flow field with laminar flow subtracted.

B. Nucleus formation

Figure 4 shows the induction time as a function of shear rate at 250 K. There are two regimes, one in which flow has no effect on the induction time, and one where the induction time decreases as a power law in the shear rate. This observation agrees with experimental results[16,77] as well as with the theoretical work by Grizzuti and co-workers.[16,78] Based on the assumption that shear can only affect nucleation if the sheared chains do not have enough time to relax back into their equilibrium structure, the crossover is expected to occur at Weissenberg number $\tau_{\max}\dot{\gamma}_c \approx 1$, where $\tau_{\max}$ is the longest relaxation time in the system, and $\dot{\gamma}_c$ is the critical shear rate, at which the induction time begins to drop. In our simulation data $\dot{\gamma}_c$ can be estimated from the intersection of the line (continuous) drawn through the induction time data at high shear rates and a horizontal line (dashed) at the value of the induction time under quiescent conditions ($\dot{\gamma} = 0$). If we assume that the center of mass diffusion of a chain across its own radius of gyration is the slowest relevant process in the system, we find $\tau_{\max}\dot{\gamma}_c = 0.6$ (where $\tau_{\max} = 1.26 \times 10^{7}\tau$), which confirms the assumption. (Here, we have used the time a chain that needs to diffuse over the length of its radius of gyration as an estimate of $\tau_{\max}$.)

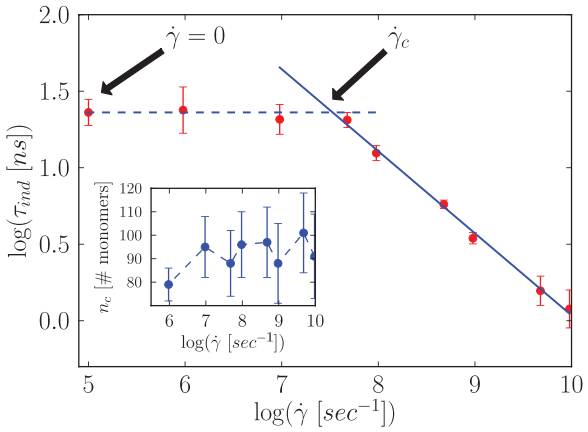

FIG. 4. Main panel: Induction time versus shear rate for C20 at 250 K. Inset: size of critical nucleus versus logarithm of shear rate.

In agreement with this interpretation, we find that at $\dot{\gamma} < \dot{\gamma}_c$ the nuclei are oriented in any random direction, while at $\dot{\gamma} > \dot{\gamma}_c$ the nuclei are oriented on average in the direction of flow, i.e., the stems are parallel to the flow field. In Fig. 5, we show the average tilt angle of the critical nucleus with respect to the flow field at different shear rates. With increasing

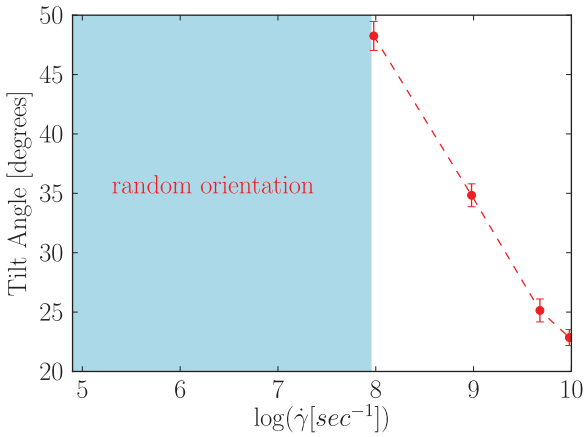

FIG. 5. C20: Average tilt angle between the critical nucleus and the flow direction versus the logarithm of the shear rate. The light blue rectangle shows that the critical nuclei are oriented in random directions as in case of quiescent conditions.

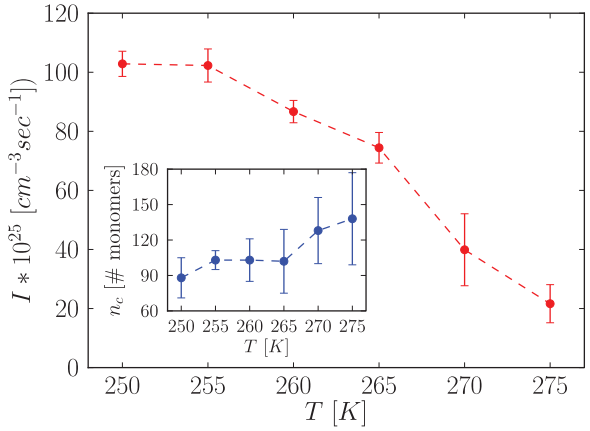

FIG. 6. Main panel: Nucleation rate versus temperature under shear flow for C20. Inset: size of the critical nucleus versus temperature.

shear rate the alignment becomes stronger (this effect is also know from experiments[79,80]). In the inset of Fig. 4, the size of the critical nucleus is plotted against the shear rate: there is no effect of shear.

Next we discuss the effect of temperature on the nucleation rate under shear flow. We carried out simulations at seven different temperatures ranging from 250 K to 280 K at a shear rate of $0.001\tau^{-1}(0.95 \times 10^9\ \text{s}^{-1})$. The integration timestep used in the simulations at 250 K was 0.005τ. Figure 6 shows the nucleation rate versus temperature. As expected, the nucleation rate decreases with increasing temperature. However, it decreases only by a factor of 5 over the temperature range from 250K to 275K. As $\gamma = 0.001\tau^{-1}$ is well above the critical shear rate, the effect of flow on the nucleation rate is stronger than the effect of temperature. The chains align primarily because they are sheared, and only secondarily because of the chemical potential difference between the bulk crystal and the bulk, metastable melt. (Again this observation is in agreement with experiments and quasi-equilibrium theories.[16,77]) In the inset of Fig. 6, we show the critical nucleus size at different degrees of supercooling. As shear is the dominating driving force for crystallization, the size of the critical nucleus depends only weakly on temperature.

To study the nucleation mechanism we analyze 10 independent trajectories for every shear rate again in terms of the average radius of gyration R_g of all chains that are part of the nucleus at t_0, the nematic order S_2 of these chains, the average volume V of the Voronoi cell associated to each particle that is part of the nucleus and its crystallinity order parameter. In Fig. 7, we show the relative variations of these quantities with respect to the values they had at $-100\Delta t$, $-70\Delta t$, $-35\Delta t$, and $-10\Delta t$, respectively, where $\Delta t = 10\,000\tau$, at shear rates $\dot\gamma = 0.00001\tau^{-1}(0.95\times10^8\ \text{s}^{-1})$, $\dot\gamma = 0.0001\tau^{-1}(0.95\times10^9\ \text{s}^{-1})$, $\dot\gamma = 0.001\tau^{-1}(0.95\times10^9\ \text{s}^{-1})$, and $\dot\gamma = 0.01\tau^{-1}(0.95\times10^{10}\ \text{s}^{-1})$, respectively. (Again, for comparison changes in the absolute magnitude of these order parameters are shown in Appendix B.) For the lowest shear rate, $\dot\gamma = 0.00001\tau^{-1}$, on approach to the formation of the critical nucleus at t_0 we observe first an increase in the global orientational order S_2, then an increase in the radius of

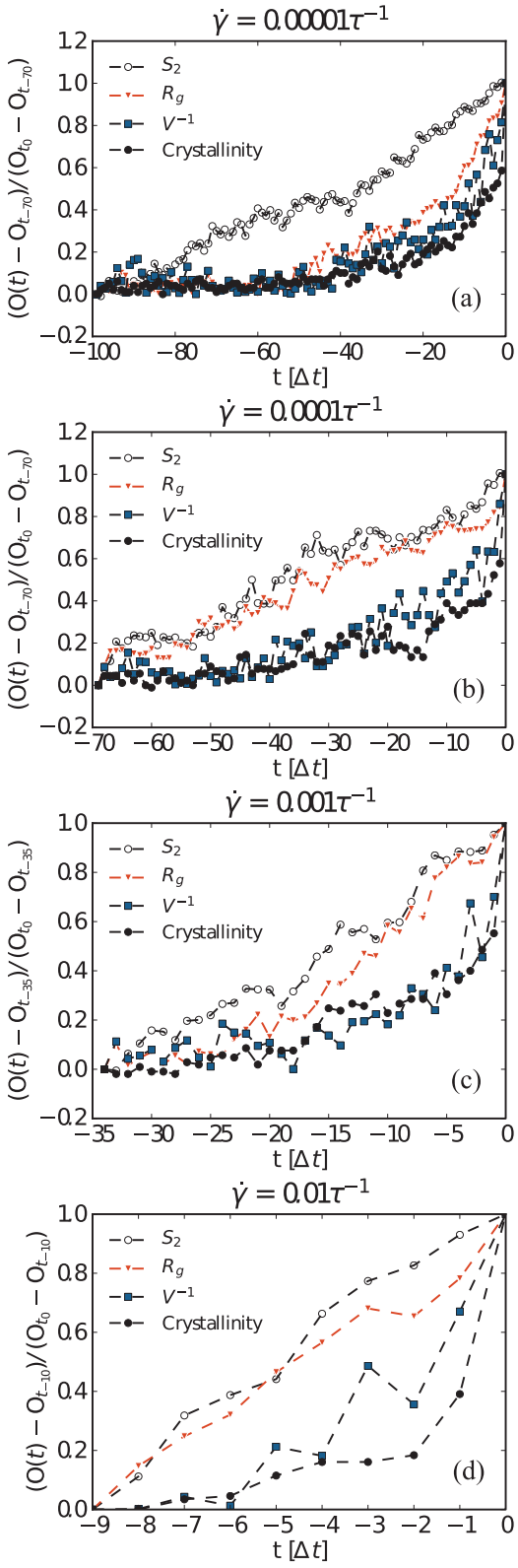

FIG. 7. C20 under shear: Relative variation of several observables (O) from the melt to the formation of a critical nucleus for the particles that are part of the critical nucleus at t_0: nematic order S_2 (black, open circles), the radius of gyration R_g (red, triangles), the inverse of the Voronoi cell volume V (blue, squares), and the crystallinity order parameter (black, closed circles). (a) $\dot\gamma = 0.00001\tau^{-1}$, (b) $\dot\gamma = 0.0001\tau^{-1}$, (c) $\dot\gamma = 0.001\tau^{-1}$, (d) $\dot\gamma = 0.01\tau^{-1}$. The curves are averaged over 10 independent trajectories progressing backwards in time from the nucleation time $t = t_0$ to $t = -100\Delta t$ at $\dot\gamma = 0.00001\tau^{-1}$, $t = -70\Delta t$ at $\dot\gamma = 0.0001\tau^{-1}$, $t = -35\Delta t$ at $\dot\gamma = 0.001\tau^{-1}$, and $t = -10\Delta t$ at $\dot\gamma = 0.01\tau^{-1}$, respectively. Here $\Delta t = 10\,000\tau$.

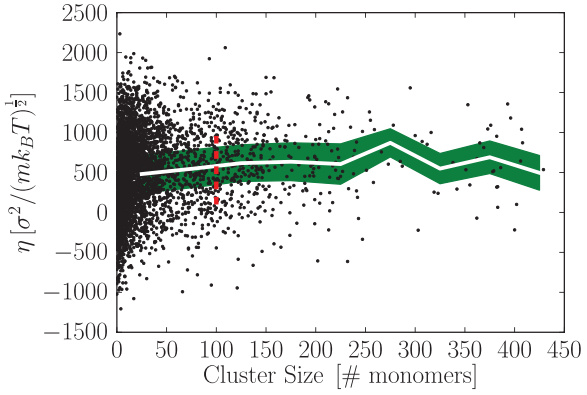

FIG. 8. C20: Shear viscosity as a function of cluster size. Simulation data points (black dots), size of the critical nucleus (red dashed line), mean value of the viscosity (white line), and its standard deviation (green envelope).

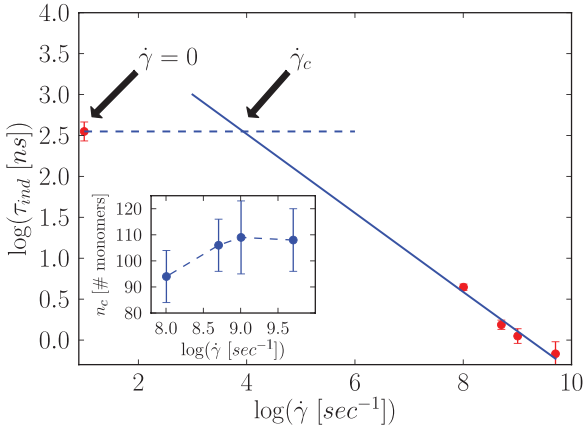

FIG. 9. Main panel: Induction time against shear rate for C150. Simulation data (red circles) and fit (blue line). Inset: Size of the critical nucleus against log of shear rate.

gyration and in the local density, and finally local positional and orientational order are established. Thus, the nucleation mechanism is the same as in the quiescent case:[40] first the chains align, then they straighten.

At $\dot\gamma = 0.0001\tau^{-1}$ and at higher shear rates, we observe a simultaneous increase in the global orientational order S_2 and in the radius of gyration R_g. This agrees with the common interpretation of $\dot\gamma_c$: when the Weissenberg number exceeds 1, the chains are straightened and oriented in the direction of flow. Thus alignment is enhanced, and the crystallization kinetics are accelerated.

We have shown that the flow field has an effect on the nucleation rate. In turn, the presence of the nucleus should also have an effect on the flow field, because the mechanical properties of a crystal differ considerably from those of the melt. In Fig. 8, we show the shear viscosity (measured using the instantaneous system average of the stress tensor) as a function of cluster size for a system consisting of 500 chains of C20, at 250 K and at a shear rate of $0.001\tau^{-1}$. The simulation data points are subject to strong fluctuations due to the small system size. We do not observe any change in the viscosity during the formation of the nucleus and growth up to a cluster size of 450 monomers. Above this cluster size the scalar pressure started to decrease, because the phase transition was simulated in the NVT ensemble. We conclude that the nucleation events do not have an effect on the flow field, as the nuclei are small for the temperatures that we discuss here.

V. C150 UNDER SHEAR

We performed simulations of 100 chains of C150, equilibrated the system at 500 K and then quenched it to 280 K. All simulations were carried out under constant volume and temperature conditions at a density of 0.89 g/cm^3. We applied shear rates $\dot\gamma$ ranging from $0.0001\tau^{-1}$ to $0.005\tau^{-1}$ ($1.012 \times 10^8\,\mathrm{s}^{-1}$ to $5.06 \times 10^9\,\mathrm{s}^{-1}$).

In Fig. 9, we show the induction time versus the shear rate. Again, the critical shear rate can be estimated as the intersection of the fitted line (continuous) at higher shear rate and a horizontal line (dashed) placed at the value of the induction time under quiescent conditions ($\dot\gamma = 0$). (The data point at $\dot\gamma = 0$ is the same as in Table I.) In the inset of Fig. 9, the size of the critical nucleus is shown versus the shear rate. It is constant within the error bars. And above $\dot\gamma_c$, the crystallites are again aligned with the flow field (Fig. 10). Thus, all results are qualitatively the same as those shown in Fig. 4 for C20. Quantitatively, however, there is a difference: if we take the time the center of mass of a chain needs to diffuse across its radius of gyration to estimate the Weissenberg number at the critical shear rate, we obtain $\tau_{\max}\dot\gamma_c = 0.41$ (where $\tau_{\max} = 2.2 \times 10^9\tau$) which is close to 1.

To identify the nucleation mechanism, we analyze 10 independent trajectories for every shear rate in terms of the order parameters that we introduced in Sec. III. In Fig. 11, we show the relative variations of these quantities with respect to the values they had at $-300\Delta t$, $-140\Delta t$, $-70\Delta t$, and $-20\Delta t$, respectively, where $\Delta t = 5000\tau$ at shear rates $\dot\gamma = 0.0001\tau^{-1}(1.012 \times 10^8\,\mathrm{s}^{-1})$, $\dot\gamma = 0.0005\tau^{-1}(5.06 \times 10^8\,\mathrm{s}^{-1})$, $\dot\gamma = 0.001\tau^{-1}(1.012 \times 10^9\,\mathrm{s}^{-1})$, and $\dot\gamma = 0.005\tau^{-1}(5.06 \times 10^{10}\,\mathrm{s}^{-1})$, respectively. (Again, for comparison changes in the absolute magnitude of these order parameters are shown in Appendix C.) For all shear rates, we observe first an increase in the nematic order S_2, then an increase in the radius of gyration, and finally the local density increases and the crystal structure with local order is formed.

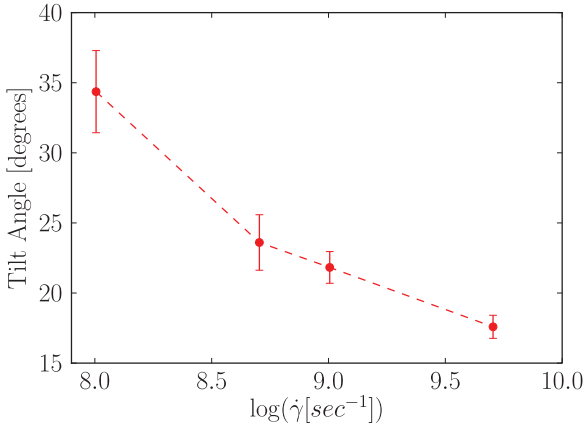

FIG. 10. C150: Tilt angle of nucleus versus shear rate.

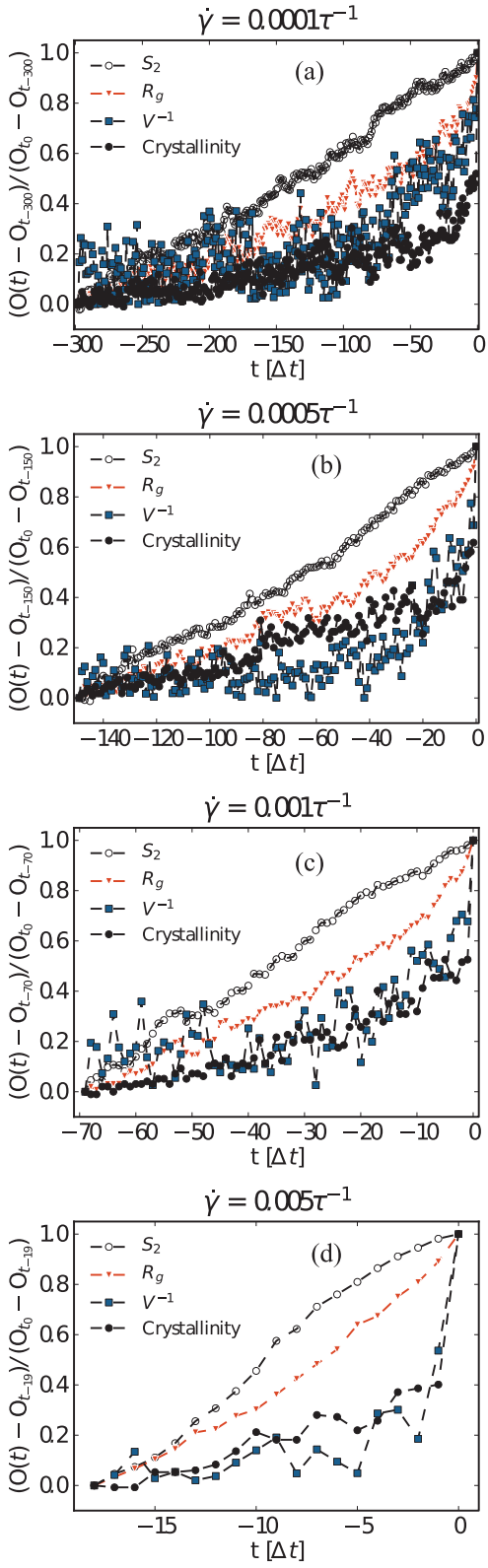

FIG. 11. C150: Relative variation of several observables (O) from the melt to the formation of a critical nucleus computed for the particles involved in the nucleus: orientational order S_2 (black, open circles), radius of gyration R_g (red, triangles), the inverse of the Voronoi cell volume V (blue, squares), and the crystallinity order parameter (black, close circles). (a) $\dot\gamma = 0.0001\tau^{-1}$, (b) $\dot\gamma = 0.0005\tau^{-1}$, (c) $\dot\gamma = 0.001\tau^{-1}$, (d) $\dot\gamma = 0.005\tau^{-1}$. The curves are averaged over 10 independent trajectories progressing backward in time from the nucleation time $t = t_0$ to $t = -300\Delta t$ at $\dot\gamma = 0.0001\tau^{-1}$, $t = -140\Delta t$ at $\dot\gamma = 0.0005\tau^{-1}$, $t = -70\Delta t$ at $\dot\gamma = 0.001\tau^{-1}$, and $t = -20\Delta t$ at $\dot\gamma = 0.005\tau^{-1}$, respectively. Here $\Delta t = 5000\tau$.

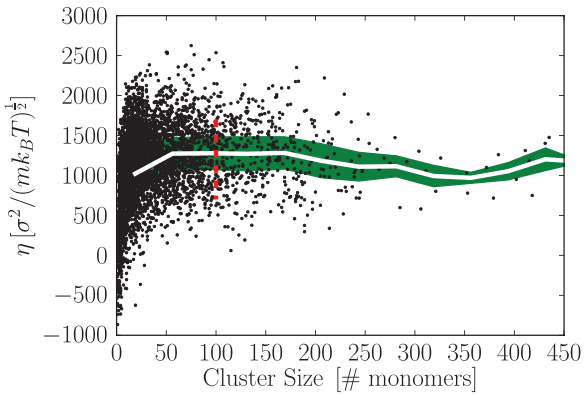

FIG. 12. C150: Shear viscosity as a function of cluster size. Simulation data points (black dots), size of the critical nucleus (red dashed line), mean value of the viscosity (white line), and its standard deviation (green envelope).

Thus for C150, the behaviour of R_g under shear differs from the quiescent case (compare to Fig. 1), but not as strongly as in C20 (see Fig. 7).

To conclude, we show in Fig. 12 the shear viscosity as a function of cluster size at a shear rate of $0.001\tau^{-1}$. Again we do not observe any change in the viscosity during the formation of the nucleus and growth up to cluster size of 450 monomers.

VI. CONCLUSIONS

We have simulated crystal nucleation from undercooled melts of short polymer chains under quiescent and shear conditions and analyzed the formation of the critical nucleus. For C150, which is longer than the entanglement length, we observe the same nucleation mechanism as for C20,[40] which is shorter than the entanglement length: under quiescent conditions, first the chain segments align, then they straighten, and finally the cluster becomes denser and local positional and orientational order are established.

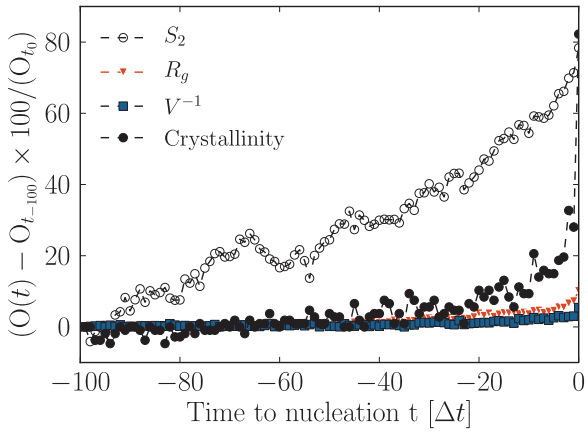

FIG. 13. Relative increase of several observables (O) from the melt to the formation of a critical nucleus, computed for those particles that are part of the nucleus at the nucleation time $t = t_0$: orientational order S_2 (black, open circles), radius of gyration R_g (red, triangles), the inverse of the Voronoi cell volume V (blue, squares), and the crystallinity order parameter (black, closed circles). The curves are averaged over 20 independent trajectories progressing backward in time from the nucleation time $t = t_0$ in steps $\Delta t = 100\,000\tau$ to $t = -100\Delta t$.

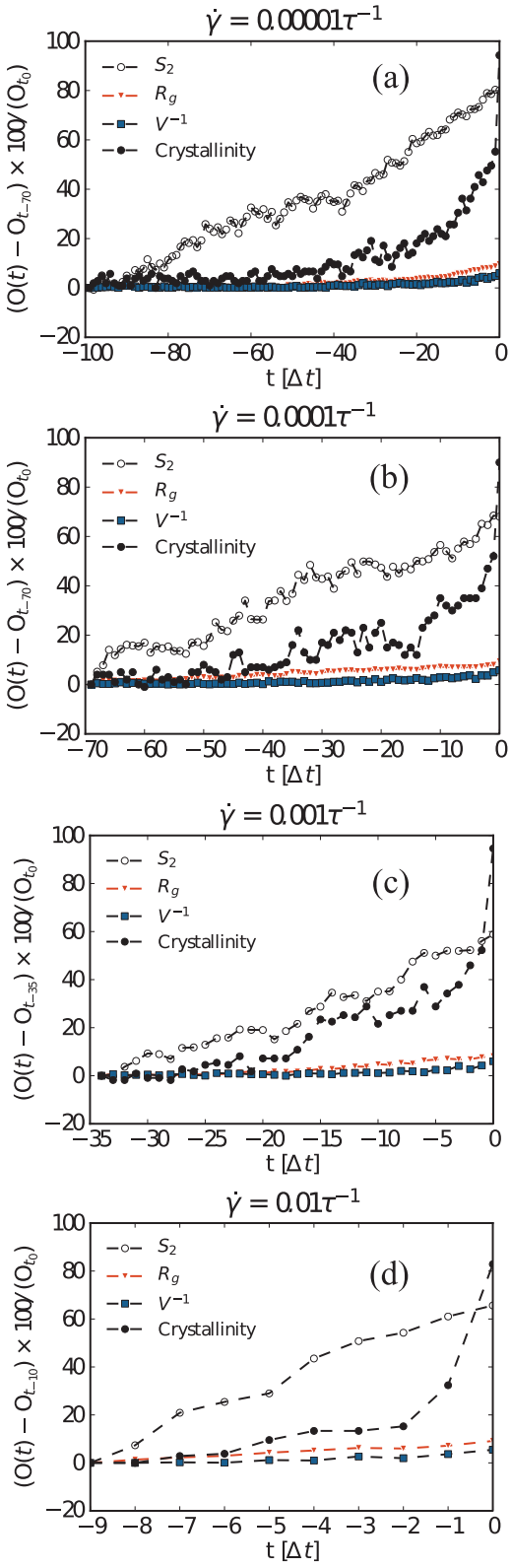

FIG. 14. Relative increase of several observables (O) from the melt to the formation of a critical nucleus for the particles that are part of the critical nucleus at t_0: nematic order S_2 (black, open circles), the radius of gyration R_g (red, triangles), the inverse of the Voronoi cell volume V (blue, squares), and the crystallinity order parameter (black, closed circles). (a) $\dot{\gamma} = 0.00001\tau^{-1}$, (b) $\dot{\gamma} = 0.0001\tau^{-1}$, (c) $\dot{\gamma} = 0.001\tau^{-1}$, (d) $\dot{\gamma} = 0.01\tau^{-1}$. The curves are averaged over 10 independent trajectories progressing backwards in time from the nucleation time $t = t_0$ to $t = -100\Delta t$ at $\dot{\gamma} = 0.00001\tau^{-1}$, $t = -70\Delta t$ at $\dot{\gamma} = 0.0001\tau^{-1}$, $t = -35\Delta t$ at $\dot{\gamma} = 0.001\tau^{-1}$, and $t = -10\Delta t$ at $\dot{\gamma} = 0.01\tau^{-1}$, respectively. Here $\Delta t = 10\,000\tau$.

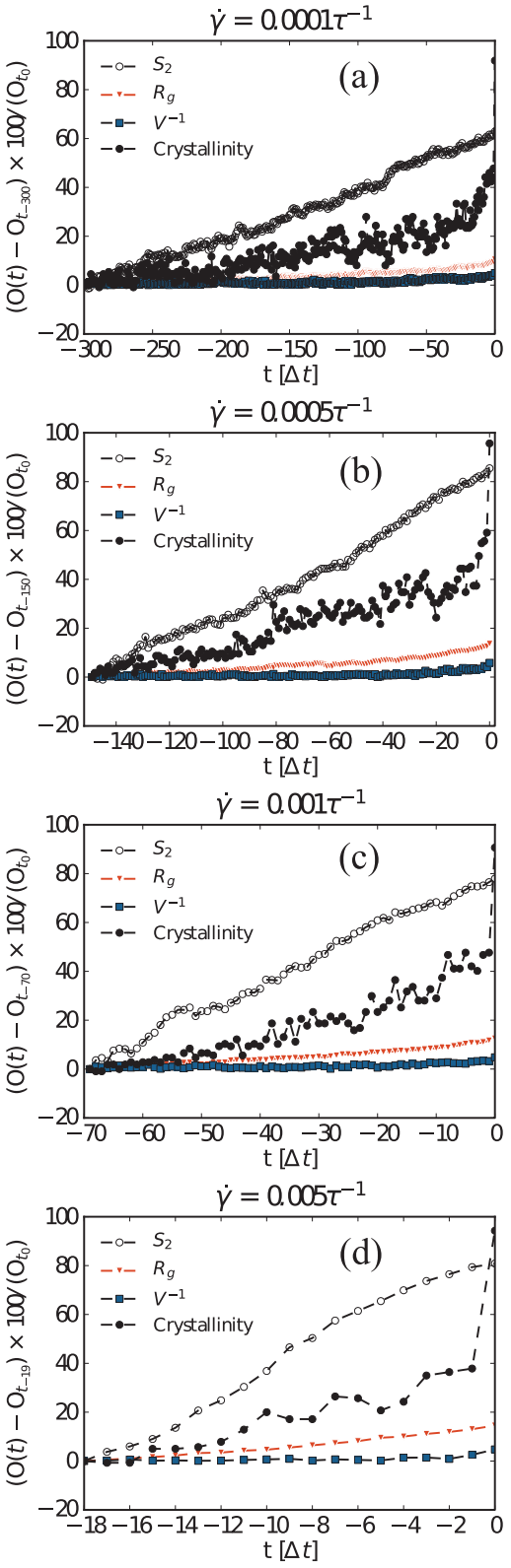

FIG. 15. Relative increase of several observables (O) from the melt to the formation of a critical nucleus computed for the particles involved in the nucleus: orientational order S_2 (black, open circles), radius of gyration R_g (red, triangles), the inverse of the Voronoi cell volume V (blue, squares), and the crystallinity order parameter (black, close circles). (a) $\dot{\gamma} = 0.0001\tau^{-1}$, (b) $\dot{\gamma} = 0.0005\tau^{-1}$, (c) $\dot{\gamma} = 0.001\tau^{-1}$, (d) $\dot{\gamma} = 0.005\tau^{-1}$. The curves are averaged over 10 independent trajectories progressing backward in time from the nucleation time $t = t_0$ to $t = -300\Delta t$ at $\dot{\gamma} = 0.0001\tau^{-1}$, $t = -140\Delta t$ at $\dot{\gamma} = 0.0005\tau^{-1}$, $t = -70\Delta t$ at $\dot{\gamma} = 0.001\tau^{-1}$, and $t = -20\Delta t$ at $\dot{\gamma} = 0.005\tau^{-1}$, respectively. Here $\Delta t = 5000\tau$.

This result might seem to be in contradiction with the work of Luo and Sommer[64] who have recently reported that nucleation preferably takes place in regions with a long entanglement length. However, their simulations have been carried out at lower degrees of undercooling than ours. We have shown results for 20%–30% undercooling, thus the critical nuclei are relatively small compared to the entanglement length. For lower degrees of undercooling and larger critical nuclei, entanglement comes into play.

At low shear rates we observe the same nucleation mechanism as under quiescent conditions. At high shear rates the chains of C20 align and straighten at the same time, then the local density increases and finally local positional and orientational order are established. In contrast, the chain segments of C150 first align and then straighten. We estimate the critical shear rates for both systems (C20 and C150) and find power law behaviour between nucleation rate and shear rate in agreement with experiments and theory.[16]

ACKNOWLEDGMENTS

We thank Francesco Turci, Jens-Uwe Sommer, Roland Sanctuary, Jörg Baller, and Carlo Di Giambattista for stimulating discussions. This project has been financially supported by the National Research Fund (FNR) within the CORE project Polyshear. Computer simulations presented in this paper were carried out using the HPC facility of the University of Luxembourg.

APPENDIX A: C150 UNDER QUIESCENT CONDITIONS

In Fig. 13, we show the relative changes in the magnitude of the order parameters for C150 under quiescent conditions. There is an 80% change in the magnitude of S_2 and the crystallinity order parameter, while the magnitude of R_g changes only by 10% and the density by 5% density from melt to crystal.

APPENDIX B: C20 UNDER FLOW

In Fig. 14, we show the relative changes in the magnitude of the order parameters for C20 under flow conditions.

APPENDIX C: C150 UNDER FLOW

In Fig. 15, we show the relative increase in the magnitude of the order parameters for C150 under flow conditions.

[1]M. Muthukumar, "Nucleation in polymer crystallization," *Advances in Chemical Physics* (John Wiley & Sons, Inc., 2004), pp. 1–63.
[2]M. Imai, K. Kaji, and T. Kanaya, Macromolecules **27**, 7103 (1994).
[3]M. Imai, K. Kaji, T. Kanaya, and Y. Sakai, Phys. Rev. B **52**, 12696 (1995).
[4]T. A. Ezquerra, E. López-Cabarcos, B. S. Hsiao, and F. J. Baltà-Calleja, Phys. Rev. E **54**, 989 (1996).
[5]A. Keller, M. Hikosaka, S. Rastogi, A. Toda, P. Barham, and G. Goldbeck-Wood, J. Mater. Sci. **29**, 2579 (1994).
[6]M. Imai, K. Mori, T. Mizukami, K. Kaji, and T. Kanaya, Polymer **33**, 4451 (1992).
[7]G. Strobl, Eur. Phys. J. E **3**, 165 (2000).
[8]G. Strobl, Eur. Phys. J. E **18**, 295 (2005).
[9]G. Strobl, Prog. Polym. Sci. **31**, 398–442 (2006).
[10]T. Y. C. G. Strobl, Eur. Phys. J. E **23**, 55 (2007).
[11]G. Strobl, Rev. Mod. Phys. **81**, 1287 (2009).
[12]R. Somani, L. Yang, I. Sics, B. Hsiao, N. Pogodina, H. Winter, P. Agarwal, H. Fruitwala, and A. Tsou, Macromol. Symp. **185**, 105 (2002).
[13]R. H. Somani, L. Yang, and B. S. Hsiao, Physica A **304**, 145 (2002).
[14]F. M. Abuzaina, B. D. Fitz, S. Andjelić, and D. D. Jamiolkowski, Polymer **43**, 4699 (2002).
[15]D. Lellinger, G. Floudas, and I. Alig, Polymer **44**, 5759 (2003).
[16]S. Coppola, L. Balzano, E. Gioffredi, P. L. Maffettone, and N. Grizzuti, Polymer **45**, 3249 (2004).
[17]A. Elmoumni and H. Winter, Rheol. Acta **45**, 793 (2006).
[18]S. Acierno and N. Grizzuti, Int. J. Mater. Form. **1**, 583 (2008).
[19]R.-C. Zhang, A. Lu, and Z.-B. Xu, J. Appl. Polym. Sci. **124**, 1562 (2012).
[20]F. J. Custódio, R. J. Steenbakkers, P. D. Anderson, G. W. Peters, and H. E. Meijer, Macromol. Theory Simul. **18**, 469 (2009).
[21]J. van Meerveld, M. Hütter, and G. W. Peters, J. Non-Newtonian Fluid Mech. **150**, 177 (2008).
[22]H. Zuidema, G. W. Peters, and H. E. Meijer, Macromol. Theory Simul. **10**, 447 (2001).
[23]S. E. M. Doi, *The Theory of Polymer Dynamics* (Oxford University Press, 1986).
[24]T. Shimada, M. Doi, and K. Okano, J. Chem. Phys. **88**, 7181 (1988).
[25]P. D. Olmsted, W. C. K. Poon, T. C. B. McLeish, N. J. Terrill, and A. J. Ryan, Phys. Rev. Lett. **81**, 373 (1998).
[26]B. M. Hongge Tan and D. Yan, J. Chem. Phys. **119**, 2886 (2003).
[27]K. Kaji, "Structure formation in PET during the induction period of crystallization," *Handbook of Thermoplastic Polyesters: Homopolymers, Copolymers, Blends, and Composites* (Wiley-VCH Verlag GmbH & Co. KGaA, 2002), pp. 225–251.
[28]R. S. Graham, A. E. Likhtman, T. C. B. McLeish, and S. T. Milner, J. Rheol. **47**, 1171 (2003).
[29]R. S. Graham and P. D. Olmsted, Phys. Rev. Lett. **103**, 115702 (2009).
[30]R. S. Graham and P. D. Olmsted, Faraday Discuss. **144**, 71 (2010).
[31]K. Jolley and R. S. Graham, J. Chem. Phys. **134**, 164901 (2011).
[32]K. Esselink, P. A. J. Hilbers, and B. W. H. van Beest, J. Chem. Phys. **101**, 9033 (1994).
[33]H. Takeuchi, J. Chem. Phys. **109**, 5614 (1998).
[34]S. Fujiwara and T. Sato, Phys. Rev. Lett. **80**, 991 (1998).
[35]S. Fujiwara and T. Sato, J. Chem. Phys. **110**, 9757 (1999).
[36]P. Yi and G. C. Rutledge, J. Chem. Phys. **131**, 1 (2009).
[37]P. Yi and G. C. Rutledge, J. Chem. Phys. **135**, 11 (2011).
[38]P. Yi, C. R. Locker, and G. C. Rutledge, Macromolecules **46**, 4723 (2013).
[39]H. Zerze, J. Mittal, and A. J. McHugh, Macromolecules **46**, 9151 (2013).
[40]M. Anwar, F. Turci, and T. Schilling, J. Chem. Phys. **139**, 214904 (2013).
[41]T. Yamamoto, J. Chem. Phys. **139**, 054903 (2013).
[42]T. Yamamoto, J. Chem. Phys. **133**, 034904 (2010).
[43]T. Yamamoto, J. Chem. Phys. **129**, 184903 (2008).
[44]T. Yamamoto, Polymer **45**, 1357 (2004).
[45]T. Yamamoto, J. Chem. Phys. **109**, 4638 (1998).
[46]C. Luo and J.-U. Sommer, Macromolecules **44**, 1523 (2011).
[47]C. Luo and J.-U. Sommer, Phys. Rev. Lett. **102**, 147801 (2009).
[48]P. Welch and M. Muthukumar, Phys. Rev. Lett. **87**, 218302 (2001).
[49]H. Meyer and F. Müller-Plathe, J. Chem. Phys. **115**, 7807 (2001).
[50]J.-U. Sommer and G. Reiter, J. Chem. Phys. **112**, 4384 (2000).
[51]N. Waheed, M. S. Lavine, and G. C. Rutledge, J. Chem. Phys. **116**, 2301 (2002).
[52]M. Muthukumar, "Modeling polymer crystallization," in *Interphases and Mesophases in Polymer Crystallization III*, Advances in Polymer Science Vol. 191, edited by G. Allegra (Springer, Berlin/Heidelberg, 2005), pp. 241–274.
[53]M. Muthukumar, Philos. Trans. R. Soc., A **361**, 539 (2003).
[54]M. Muthukumar, Eur. Phys. J. E **3**, 199 (2000).
[55]A. Koyama, T. Yamamoto, K. Fukao, and Y. Miyamoto, Phys. Rev. E **65**, 050801 (2002).
[56]A. Koyama, T. Yamamoto, K. Fukao, and Y. Miyamoto, J. Macromol. Sci., Part B **42**, 821 (2003).
[57]M. S. Lavine, N. Waheed, and G. C. Rutledge, Polymer **44**, 1771 (2003).
[58]M. J. Ko, N. Waheed, M. S. Lavine, and G. C. Rutledge, J. Chem. Phys. **121**, 2823 (2004).
[59]T. C. Ionescu, C. Baig, B. J. Edwards, D. J. Keffer, and A. Habenschuss, Phys. Rev. Lett. **96**, 037802 (2006).
[60]A. Jabbarzadeh and R. Tanner, J. Non-Newtonian Fluid Mech. **160**, 11 (2009).

[61]I. Dukovski and M. Muthukumar, J. Chem. Phys. **118**, 6648 (2003).
[62]C. Baig and B. J. Edwards, J. Non-Newtonian Fluid Mech. **165**, 992 (2010).
[63]C. Baig and B. J. Edwards, Europhys. Lett. **89**, 36003 (2010).
[64]C. Luo and J.-U. Sommer, Phys. Rev. Lett. **112**, 195702 (2014).
[65]W. Paul, D. Y. Yoon, and G. D. Smith, J. Chem. Phys. **103**, 1702 (1995).
[66]N. Waheed, M. Ko, and G. Rutledge, Polymer **46**, 8689 (2005).
[67]H. J. Limbach, A. Arnold, B. A. Mann, and C. Holm, Comput. Phys. Commun. **174**, 704 (2006).
[68]J. Qin and S. T. Milner, Soft Matter **7**, 10676 (2011).
[69]R. S. Hoy, K. Foteinopoulou, and M. Kröger, Phys. Rev. E **80**, 031803 (2009).
[70]G. Subramanian and S. Shanbhag, J. Chem. Phys. **129**, 144904 (2008).
[71]M. Tanaka, K. Iwata, and N. Kuzuu, Comput. Theor. Polym.Sci. **10**, 299 (2000).
[72]A. Kolb and B. Dünweg, J. Chem. Phys. **111**, 4453 (1999).
[73]J. Wedekind, R. Strey, and D. Reguera, J. Chem. Phys. **126**, 134103 (2007).
[74]C. H. Rycroft, Chaos **19**, 041111 (2009).
[75]T. Soddemann, B. Dünweg, and K. Kremer, Phys. Rev. E **68**, 046702 (2003).
[76]A. Chatterjee, Mol. Simul. **33**, 1233 (2007).
[77]M. Derakhshandeh and S. Hatzikiriakos, Rheol. Acta **51**, 315 (2012).
[78]G. Marrucci and N. Grizzuti, J. Rheol. **27**, 433 (1983).
[79]E. Manias, "A computer simulation study nanorheology of strongly confined molecular fluids," Ph.D. thesis (State University of Groningen, 1995).
[80]G. H. Peters and D. J. Tildesley, Phys. Rev. E **52**, 1882 (1995).